A joint microlensing analysis of lensing mass and accretion disc models

Vernardos, G.

IMPORTANT NOTE: You are advised to consult the publisher's version (publisher's PDF) if you wish to cite from it. Please check the document version below.

Document Version
Publisher's PDF, also known as Version of record

Publication date:
2018

[Link to publication in University of Groningen/UMCG research database](#)

A joint microlensing analysis of lensing mass and accretion disc models

G. Vernardos⋆

Kapteyn Astronomical Institute, University of Groningen, PO Box 800, NL-9700AV Groningen, the Netherlands

ABSTRACT

Microlensing of multiply imaged quasars is a unique probe of quasar structure, down to the size of the accretion disc and the central black hole. Flux ratios between close pairs of images of lensed quasars can be used to constrain the accretion disc size and temperature profile. The starting point of any microlensing model is the macromodel of the lens, which provides the convergence and shear values at the location of the multiple images. Here I present a new approach of microlensing modelling independently of the macromodel of the lens. The technique is applied to the close pair of images A_1 and A_2 of MG 0414+0534, for a set of flux ratios with large variation with respect to wavelength. The inferred accretion disc size and temperature profile measurements, as well as the smooth matter fraction at the location of the images, are quite robust under a wide range of macromodel variations. A case of using purely microlensing data (flux ratios) to constrain the macromodel is also presented. This is a first application of the technique on a fiducial system and set of flux ratios; the method is readily applicable to collections of such objects and can be extended to light-curve and/or imaging data.

Key words: accretion, accretion discs – gravitational lensing: micro – gravitational lensing: strong – quasars: individual: MG 0414+0534.

1 INTRODUCTION

Cosmological microlensing observations constitute a unique probe of the structure of lensing galaxies and lensed quasars. Understanding the dark (smooth) and stellar (compact) matter components in galaxy-scale systems is an open issue and has many implications for studying their formation and evolution scenarios (e.g. Conroy & Wechsler 2009; Behroozi, Conroy & Wechsler 2010; Moster et al. 2010). To this end, using strong gravitational lenses has been valuable (e.g. Treu et al. 2010; Oguri, Rusu & Falco 2014; Leier et al. 2016).

In the case of the lensed source being a quasar, microlensing can be employed to unveil the structure of the accretion disc and the geometry of the emitting regions in the vicinity of the supermassive black hole (e.g. Dai et al. 2010; Morgan et al. 2010; Guerras et al. 2013; O'Dowd et al. 2015). This, in turn, can be used to understand the growth of the black hole (e.g. Rosas-Guevara et al. 2015; Terrazas et al. 2017) and its relation to the quasar host galaxy and its environment via feedback mechanisms (e.g. Bourne & Sijacki 2017; Cowley et al. 2018).

For any quasar to be microlensed, it has to be first multiply imaged by a foreground lensing galaxy (the 'macrolens', or just 'lens'). The positions of the images, any extended lensed features of the background quasar host galaxy, and other available data (e.g. time delays

or flux ratios between the images) can be used to construct a mass model for the lens (e.g. see Keeton 2001). Such models describe the total mass of the lens, and provide the convergence, κ, and shear, γ, fields. However, the degeneracy between its baryonic and dark matter components remains. To lift this degeneracy, the light profile of the lens can be used to measure the smooth matter fraction, s (equation 5), as a function of radius (Oguri et al. 2014; Foxley-Marrable et al. 2018). This approach, however, is accompanied by the large uncertainty in the stellar initial mass function, used to convert the light into the mass distribution. The individual values of κ, γ, and s, at the locations of the multiple images are the primary parameters for setting the microlensing properties.

Incoming light rays from the background quasar are further deflected by several stellar-mass microlenses existing within the lens and lying along the line of sight to the quasar images. The presence of such collective deflections creates a network of caustics which can be described by a magnification map (Kayser, Refsdal & Stabell 1986). The properties of these maps (e.g. the caustic density, orientation, etc) depend mainly on κ, γ, and s, which set the mass density of the essential grainy (i.e. stellar in this case) mass component. The final result is a microlensing-induced time-dependent magnification on the source, uncorrelated between its observed (macro) images. Analysing observations using microlensing techniques can provide a measurement for s (Schechter & Wambsganss 2002), which can otherwise be only approximated as explained in the previous paragraph. This has been done using microlensing light-curve data (e.g. Chartas et al. 2009; Dai et al. 2010; MacLeod et al. 2015) or mi-

⋆ E-mail: gvernard@astro.rug.nl

crolensing flux ratios (e.g. Bate et al. 2011; Pooley et al. 2012; Jiménez-Vicente et al. 2015).

Besides κ, γ, and s, the size of the source with respect to the caustics plays an important role: the smaller the background source, the more prominent the microlensing induced brightness variations will be. It is currently thought that quasar accretion discs are hotter in their innermost regions and cool down further from the central supermassive black hole. The standard thin-disc model (Shakura & Sunyaev 1973) predicts a power-law dependence of the temperature as a function of radius, with the power-law index fixed to 3/4. This is easily transformed into a size–wavelength relation, making discs appear bigger in long (red) and smaller in short (blue) wavelengths. This wavelength-dependent microlensing effect has been used to constrain quasar accretion discs (Bate et al. 2008; Floyd, Bate & Webster 2009; Jimenez-Vicente et al. 2014; Rojas et al. 2014; Bate et al. 2018).

All microlensing studies so far have employed the 'traditional' two-stage modelling approach. First, a lens mass model is fitted to the imaging data and the individual values of κ, γ are extracted for each image. Secondly, a set of microlensing magnification maps is produced as a function of s (or other parameters like the microlens masses, proper motions, etc). A series of flux ratios or light curves are produced from the maps for different accretion disc profiles and compared to the observations (in the case of light curves, the time delay between the macro-images has to be used to correct the data first). The very high computational cost associated with generating magnification maps for different parameters (Bate & Fluke 2012), and the adequately constrained lens mass models from imaging data justify the choice of using fixed values for κ, γ.

The possibility of inferring microlensing constraints, and their robustness, on the lens mass model has not been investigated before. Conversely, studies of the effect of lens model variations/uncertainties on accretion disc constraints, or s, inferred by microlensing have been very limited (e.g. see Vernardos & Fluke 2014b). The main reason behind this is the computationally demanding task of producing magnification maps for many different combinations of κ, γ, and s.

The new approach presented in this work assesses the robustness of the derived s and accretion disc constraints with respect to the lens-mass model (i.e. the κ, γ). The feasibility of using purely microlensing data and methods in providing constraints to the lens-mass model is also examined. Any constraints on κ, γ coming from the macromodel (i.e. having them as fixed parameters) are therefore dropped, and they are treated as free parameters instead. Although a computationally more intensive task as a whole, the bulk of the effort, which is computing magnification maps, can be avoided by using the GERLUMPH[1] collection of maps (Vernardos et al. 2014; Vernardos & Fluke 2014a), whose uniform and extensive coverage of the κ, γ, and s parameter space makes it ideal for such an application. The model and its implementation, as well as the choice of a fiducial system to apply it, are described in Section 2. Results are presented in Section 3, followed by discussion and conclusions in Section 4.

2 METHOD

The geometry of the multiple images of a lensed source is well understood and can be reproduced by relatively simple elliptical mass models. Understanding the absolute brightness of the individual images is a more complicated task: one has to know the intrinsic brightness of the source, its variability, and the time delays between the images, which are much more sensitive to the exact lensing mass configuration (Kochanek et al. 2006). Although these effects can be mitigated by using the relative brightness, i.e. the flux ratios of the images, one still has to take into account microlensing and substructure in the lens (Mao & Schneider 1998; Metcalf & Madau 2001). In the absence of such contaminating effects, lensing theory provides a useful result: close image pairs in a fold configuration are expected to have magnifications of roughly the same magnitude (Schneider, Kochanek & Wambsganss 2006) and therefore an expected magnification ratio of unity (a similar rule holds for a cusp configuration of the images).

The new technique presented in Section 2.1 is applied to one such system, i.e. the close image pair of MG 0414+0534, introduced in Section 2.2. This pair, as expected, consists of a saddle point (A_2) and a minimum (A_1) image, which are labelled accordingly in the following. The specific details of applying the model to the data are presented in Section 2.3.

2.1 Model description

The new approach introduced in this work consists of allowing the κ, γ values for the images to vary. The relative contribution of the smooth component to the total mass density is assumed to be the same for both images. This assumption is justified by the close separation of the image pair and its azimuthal orientation around the centre of the lens (i.e. the images are found at roughly the same direction and distance from the lens centre). This approximation has been widely used in the literature (e.g. Bate et al. 2011; Jimenez-Vicente et al. 2014; Bate et al. 2018) as it greatly facilitates the computations, and, to first order, produces meaningful results.

The size of the accretion disc as a function of wavelength is given a parametric power-law form

$$r = r_0 \left(\frac{\lambda}{\lambda_0} \right)^\nu, \tag{1}$$

where r_0 is the size at the fiducial wavelength $\lambda_0 = 1026$ Å, which together with the power-law index, ν, constitute the two free parameters of the disc model. The size r is matched to the half-light radius, $r_{1/2}$, of a circularly symmetric (face-on) Gaussian brightness profile for the source.[2] The absolute values of the brightness are unimportant because, as explained above, only flux ratios are examined in this work.

The general form of the Bayesian posterior probability distribution is

$$P(\boldsymbol{p}|\boldsymbol{d}, \boldsymbol{\eta}) = \frac{L(\boldsymbol{d}|\boldsymbol{\eta}, \boldsymbol{p})Pr(\boldsymbol{p})}{E(\boldsymbol{d}|\boldsymbol{\eta})}, \tag{2}$$

where $\boldsymbol{p}$ is the vector of the free parameters for this model ($\kappa_{\min}$, $\gamma_{\min}$, κ_{sad}, γ_{sad}, s, r_0, ν), and $\boldsymbol{d}$ is the data from Table 1. $\boldsymbol{\eta}$ is a vector of parameters that we may choose to keep fixed (either $\kappa_{\min}$, $\gamma_{\min}$, or κ_{sad}, γ_{sad}, see Section 3; other parameters that one may wish to keep track of could be added here, e.g. the average mass of the microlenses, etc) and is omitted in the rest. Pr is the prior

---

[1]http://gerlumph.swin.edu.au

[2]Mortonson, Schechter & Wambsganss (2005) have shown that the actual shape of such a profile does not play an important role, and it is the size of the half-light radius that matters for the purposes of microlensing.

Table 1. Flux ratios between images A_2 and A_1 of MG 0414+0534 as a function of observed wavelength, λ, adopted from Bate et al. (2018).

λ (Å)	A_2/A_1
7612	0.34 ± 0.03
8436	0.42 ± 0.02
12486	0.66 ± 0.01
15369	0.76 ± 0.01

probability of the parameters $\boldsymbol{p}$, and E is the Bayesian evidence. The likelihood term, L, for a fixed set of parameters $\boldsymbol{p}$ is given by

$$L(\boldsymbol{d}|\boldsymbol{p}) = \sum_{k=1}^{N} L_k = \sum_{k=1}^{N} \exp\left(-\frac{\chi_k^2}{2}\right), \qquad (3)$$

as the sum over all the chi-squared realizations

$$\chi_k^2 = \sum_{i=1}^{4} \left(\frac{f_i^{\mathrm{obs}} - f_{i,k}^{\mathrm{sim}}}{\sigma_i}\right)^2, \qquad (4)$$

where the index i corresponds to the observed flux ratios, f^{obs}, and their uncertainties, σ, as a function of wavelength, and the index k corresponds to our simulated flux ratios, f^{sim}. Obtaining f^{sim}, the strategy of finding L as a function of the free parameters $\boldsymbol{p}$, and the priors used are described in the next sections.

2.2 The close pair of MG 0414+0534

The new approach presented here is applied to images A_1 (minimum) and A_2 (saddle point) of the quadruply imaged quasar MG 0414+0534 which have a separation of $\delta\theta \approx 0.4$ arcsec (Hewitt et al. 1992). Due to a deviation (anomaly) from the expected magnification ratio of unity in the UV and optical, which persists in infrared and radio observations (where any microlensing effect is expected to be negligible), this particular system has been the focus of several studies of possible substructure in the lens (Mao & Schneider 1998; Dalal & Kochanek 2002; Minezaki et al. 2009; MacLeod et al. 2013).

Additionally, a number of microlensing analyses have been performed on this system: Bate et al. (2008, 2011) and Blackburne et al. (2011) find a temperature profile of the quasar accretion disc which is consistent with the thin-disc model, while Pooley et al. (2007) find a size larger than expected. Recently, Bate et al. (2018) have used *Hubble Space Telescope* (*HST*) data to measure an accretion disc with size $\ln(r_0) < 1.07$ (r_0 in light days) and slope $\nu = 2.1^{+0.6}_{-0.6}$ (modelled after equation 1), marginally larger than thin disc theory expectations.

In this study, we adopt the microlensing flux ratio data obtained by Bate et al. (2018), shown in Table 1. We also use the macromodel of MacLeod et al. (2013; table 3), which consists of three components: the main lens, modelled as a singular isothermal ellipsoid (SIE) with external shear, a known companion galaxy, modelled as a singular isothermal sphere (SIS), and an unknown (dark) substructure, also modelled as a SIS. Based on this macromodel, Bate et al. (2018) computed the values of the convergence and the shear of each image in the pair, hereafter referred to as κ_{ML13}, γ_{ML13} (see Table 2).

Based on the data of Bate et al. (2018), the macromodel of MacLeod et al. (2013), and general properties of close image pairs, the following remarks/simplifications can be made. First, the time delay between the images is expected to be very short (e.g. see Pooley et al. 2007; for an analysis of 10 systems, including MG 0414+0534), and so the quasar can be essentially considered in the

same state for both images at the time of observation. Secondly, the flux in each filter that is coming from regions (and physical scales) beyond the accretion disc (and thus effected differently by microlensing) is minimal; this has been achieved by carefully selecting which *HST* filters to observe with (see fig. 1 of Bate et al. 2018). Thus, in the following, the wavelength dependence of the flux ratios is attributed solely to the structure of the quasar accretion disc and its ongoing microlensing. Lastly, as explained above, in the case of an unperturbed lens-mass model and without any differential extinction, the expected magnification ratio would be equal to unity. However, the presence of substructure in the lens (MacLeod et al. 2013) and/or the possible effect of differential extinction (which is harder to correct for as it requires spectroscopic data, e.g. Jimenez-Vicente et al. 2014; O'Dowd et al. 2015) are causing deviations from unity. These effects are taken into account by setting a baseline magnification ratio of $f_{\mathrm{base}} = 0.93 \pm 0.03$, assumed to be unaffected by microlensing. This was obtained from the infrared observations and subsequent models of Minezaki et al. (2009) and MacLeod et al. (2013).

2.3 Implementation

The macromodel, or lens, parameters consist of the convergences and shears, $\kappa_{\min}$, $\gamma_{\min}$, κ_{sad}, γ_{sad}, and the smooth matter fraction, s, assumed to be the same for both images. The accretion disc parameters are the size, r_0, and power-law slope, ν. Thus, the model can have up to a total of seven free parameters. For the macromodel parameters we adopt the ranges $0 < \kappa < 1$, $0 < \gamma < 1.4$, and $0 \le s \le 0.9$ (the last one in steps of 0.1). Magnification maps were retrieved from the full GERLUMPH[3] data set (see fig. 4 of Vernardos & Fluke 2014a; and related text for details). The Einstein radius on the source plane, R_{Ein}, is set to 3.74×10^{16} cm for microlenses with a fixed mass of $1\,M_\odot$, using $z_S = 2.64$ (Lawrence et al. 1995) and $z_L = 0.96$ (Tonry & Kochanek 1999) for the measured redshifts of the source and the lens, and a Universe with $H_0 = 70\,\mathrm{km\,s^{-1}\,Mpc^{-1}}$, $\Omega_m = 0.3$, and $\Omega_\Lambda = 0.7$. For the accretion disc parameters a regular grid is selected such that $\ln(r_0) = 0.3 \times j$ for $j = 0\ldots 11$ and $\nu = 0.25 \times i$ for $i = 0\ldots 15$, following Jimenez-Vicente et al. (2014).

The remaining procedure is almost identical to the one presented in Bate et al. (2018). For each combination of $\ln(r_0)$ and ν, a set of two-dimensional, symmetric, face-on, Gaussian profiles (see Mortonson et al. 2005) are generated for the accretion disc in each wavelength of Table 1. The half-light radius of each profile is $r_{1/2} = 1.18r$, where r comes from equation (1), i.e. it is the standard deviation of the Gaussian. The profiles are truncated at $2 \times r_{1/2}$, having a total width of $4 \times r_{1/2}$. Whenever a profile has a total width larger than $16\,R_{\mathrm{Ein}}$[4] it is regarded as being too large to be affected by microlensing and the flux ratio is assumed to have the baseline value f_{base}.

For the rest of the profiles, in order to get the simulated flux ratios, f^{sim}, to be used in equation (4), a convolution with each magnification map has to be carried out first. Due to the convolution edge effects, instead of the entire convolved maps only a central 'effective' part of them is used. The size of this effective map is

---

[3] Both GD1 and GD3 data sets were used, which are computed on a regular but sparse and an irregular but dense κ, γ grid, respectively. All the maps are available online at: http://gerlumph.swin.edu.au

[4] This limit is debatable as the caustics can still have a structure on this scale, depending on the values of κ, γ, and thus there could be still some microlensing effect present. See also the discussion in Section 4.

Table 2. Expectation values for the macromodel (κ, γ, s) and accretion disc ($\ln(r_0)$), ν) parameters at the 68 per cent confidence interval for the four sets of results introduced in Section 3. The size parameter r_0 is measured in light days. The κ, γ values for REF are based on MacLeod et al. (2013). Values that are shown without uncertainties are kept fixed.

| | REF (both fixed) | CON6 (one free) | | CON7 (one constrained) | | CON8 (both varying) |
		Minimum	Saddle point	Minimum	Saddle point	
$\kappa_{\min}$	0.51	$0.41^{+0.17}_{-0.21}$	0.51	$0.18^{+0.19}_{-0.11}$	0.51	$0.42^{+0.26}_{-0.30}$
$\gamma_{\min}$	0.42	$0.23^{+0.27}_{-0.17}$	0.42	$0.74^{+0.12}_{-0.23}$	0.42	$0.83^{+0.05}_{-0.30}$
κ_{sad}	0.56	0.56	$0.41^{+0.36}_{-0.29}$	0.56	$0.17^{+0.21}_{-0.12}$	$0.50^{+0.34}_{-0.36}$
γ_{sad}	0.51	0.51	$1.09^{+0.14}_{-0.27}$	0.51	$0.86^{+0.10}_{-0.18}$	$0.90^{+0.07}_{-0.28}$
s	$0.61^{+0.21}_{-0.24}$	$0.65^{+0.18}_{-0.38}$	$0.47^{+0.28}_{-0.31}$	$0.66^{+0.18}_{-0.38}$	$0.53^{+0.25}_{-0.28}$	$0.62^{+0.20}_{-0.34}$
$\ln(r_0)$	≤ 1.00	≤ 0.86	$0.85^{+0.59}_{-0.53}$	≤ 0.79	≤ 0.82	≤ 0.92
ν	$1.65^{+0.50}_{-0.52}$	$1.63^{+0.53}_{-0.60}$	$1.59^{+0.54}_{-0.52}$	$1.57^{+0.55}_{-0.56}$	$1.65^{+0.52}_{-0.57}$	$1.64^{+0.50}_{-0.52}$

determined by the largest profile, i.e. the one in the reddest wavelength $\lambda = 15369$ Å, e.g. for $\ln(r_0)$, $\nu = (0.3, 1)$ equation (1) gives $r = 5.23 \times 10^{16}$ cm $\approx 1.4 R_{\text{Ein}}$ and the effective map size is $18.4 R_{\text{Ein}}$ (from the 25 R_{Ein} GERLUMPH maps). Magnification values are drawn from a square grid of 10^4 points in each effective map, producing 10^8 simulated flux ratios in each wavelength. Hence, first the χ^2 term of equation (4) is calculated, and then the sum of equation (3), that has $N = 10^8$ terms, is computed.

The analysis and results presented below are based on relative posterior probabilities, therefore, the computationally demanding calculation of the evidence term in equation (2) is disregarded. Such a computation would be meaningful in the case of comparisons between different physically motivated models for the lens or the disc, which is feasible within the general formulation introduced above, but out of the scope of this paper. Because of this, the terms likelihood and probability are used interchangeably in the following. Fixed grids are adopted for the exploration of the parameter space, leaving the use of other, more elaborate and efficient sampling techniques, such as Markov Chains, Gibbs sampling, or other optimizers, for future work.

Finally, all the priors were chosen to be flat, except for r_0 that has a logarithmic prior (Bate et al. 2018). One could argue that s should have a logarithmic prior as well, since it is a multiplicative parameter

$$\kappa_* = (1 - s)\kappa, \tag{5}$$

where κ_* is the convergence in compact matter. In the next section the results were computed using both priors for s.

3 RESULTS

The model presented in the previous section has a total of seven free parameters ($\kappa_{\min}$, $\gamma_{\min}$, κ_{sad}, γ_{sad}, s, r_0, ν). A completely unconstrained variation of the κ, γ values for both images, together with the rest of the parameters, is a computationally demanding task, especially when using fixed grids to explore the parameter space. The results presented in this section are divided into sets having different constraints. The flux ratio data, shown in Table 1, are used in all cases and provide four constraints to the model. The κ, γ of each, or both, of the images, are allowed to vary freely or under some constraint:

(i) REF: this is a benchmark, or reference, set, keeping both $\kappa_{\min}$, $\gamma_{\min}$ and κ_{sad}, γ_{sad} fixed to the corresponding κ_{ML13}, γ_{ML13} values (the number of constraints is 8). The same parameter values and setup are used as in Bate et al. (2018).

(ii) CON6 allowing either $\kappa_{\min}$, $\gamma_{\min}$ or κ_{sad}, γ_{sad} to vary freely in the parameter space while keeping the other fixed to the κ_{ML13}, γ_{ML13} values (the number of constraints is 6).

(iii) CON7: same as in the previous set, but in this case the varying κ, γ are constrained by equation (6) in order to reproduce the magnification given by the κ_{ML13}, γ_{ML13} values (the number of constraints is 7).

(iv) CON8: varying both $\kappa_{\min}$, $\gamma_{\min}$ and κ_{sad}, γ_{sad} under the constraint of reproducing the magnification given by the κ_{ML13}, γ_{ML13} values (using equation 6) and matching to a given slope of a fiducial spherical potential for the lens (using equation 11; the number of constraints is 8).

The magnification is obtained from the lens equation (e.g. see Schneider et al. 2006) as

$$\mu = \frac{1}{(1 - \kappa)^2 - \gamma^2}. \tag{6}$$

This equation is used to define the critical line, i.e. the locus of points in the κ, γ plane, corresponding to a straight line, where the magnification goes to infinity. The critical line serves also as a division between the minimum ($\mu > 0$) and saddle-point ($\mu < 0$) regions of the parameter space (see Fig. 1).

In the left-hand panel of Fig. 1, we show the probability surface from equation (2) as a function of $\kappa_{\min}$, $\gamma_{\min}$ and κ_{sad}, γ_{sad}, respectively, marginalized over the remaining parameters s, r_0, and ν (CON6). This is equivalent to the likelihood surface of equation (3) under the use of flat priors and examining relative probability values. A total of 140 (300) combinations of $\kappa_{\min}$, $\gamma_{\min}$ (κ_{sad}, γ_{sad}) is shown, selected randomly in the parameter space. The resulting grid is irregular and a generic 'pixel' needs to be associated with each probed location. Here, the κ, γ plane is partitioned in Voronoi cells, which enclose the points closer to a specific probed location than to any other location. Another choice of partitioning could be the Delaunay triangulation, however, this would associate three grid points rather than one, as is the case with a Voronoi cell that is closer to the notion of a pixel centred on a measurement. The Voronoi and Delaunay tessellations are the dual of each other, and are unique. For further marginalization over either κ or γ (e.g. to obtain the expectation values and confidence intervals shown in Table 2), the likelihood is weighted by the area of each Voronoi cell.

The transformation provided by Paczynski (1986)

$$\kappa_{\text{eff}} = \frac{(1 - s)\kappa}{1 - s\kappa}, \quad \gamma_{\text{eff}} = \frac{\gamma}{1 - s\kappa}, \tag{7}$$

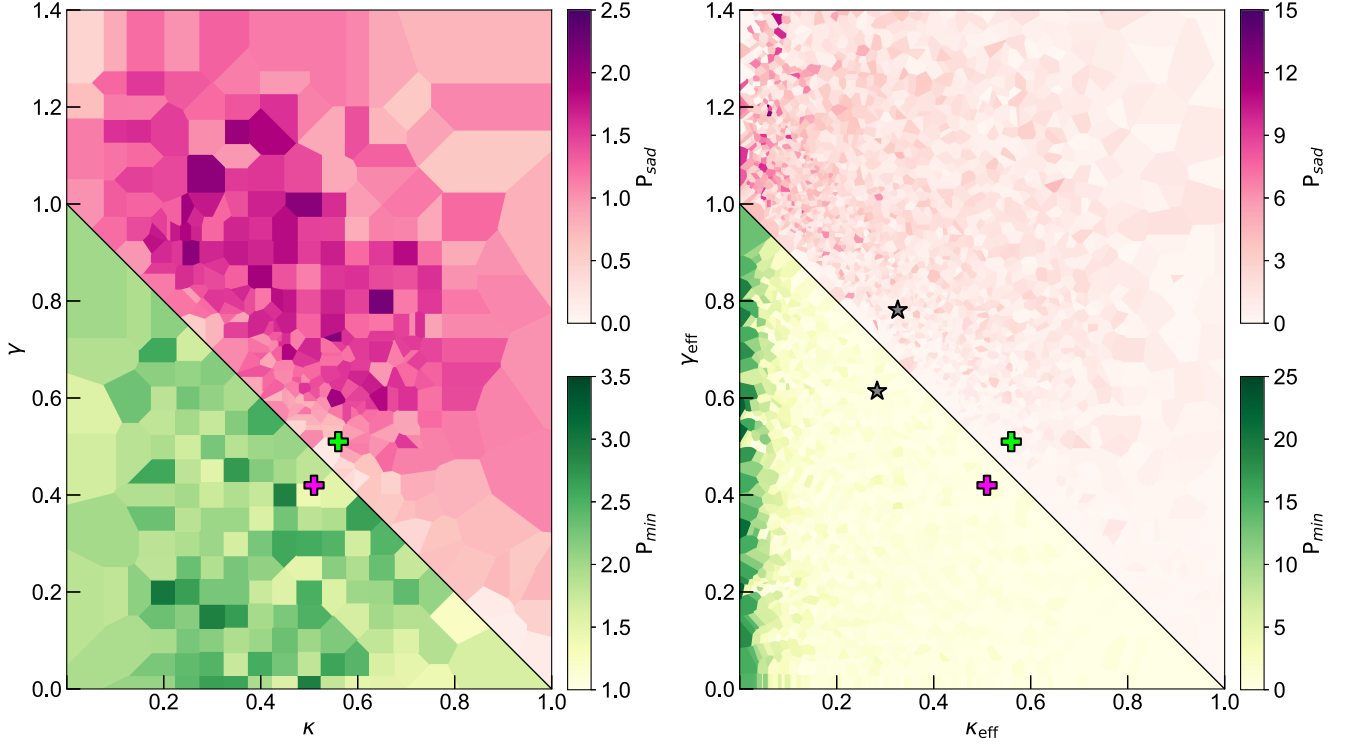is a consequence of the mass-sheet degeneracy (Falco, Gorenstein & Shapiro 1985), and reduces the three macromodel parameters κ, γ,

Figure 1. Results for CON6. Left: $\kappa-\gamma$ joint probability density marginalized over s, r_0, and ν, plotted as shaded Voronoi cells, with a darker (lighter) colour indicating a higher (lower) probability. Right: probability density for κ, γ, s, marginalized over the accretion disc parameters r_0 and ν, shown in the effective parameter space (using the transformation of equation 7). The parameter space in each panel is divided by the critical line (black solid line, see also equation 6) separating the saddle point and minimum regions, above and below it, respectively. The likelihood surface shown for the saddle point is computed while keeping the minimum image fixed to its κ_{ML13}, γ_{ML13} values (indicated by a cross) and vice versa. The locations of the effective κ_{ML13}, γ_{ML13} are also marked (grey stars), using the value of $s = 0.61$ from Table 2 (for REF).

s to only two: the effective convergence, κ_{eff}, and shear, γ_{eff}, where κ_{eff} is now due only to compact microlenses. This transformation allows the collapsed likelihood,[5] shown in the left-hand panel of Fig. 1 as a function of κ, γ, to be shown as a function of κ_{eff}, γ_{eff} in the right-hand panel of the same figure. The transformation introduces a weighting of the probability density by the determinant of its Jacobian matrix

$$\left| \det \frac{\partial(\kappa, \gamma)}{\partial(\kappa_{eff}, \gamma_{eff})} \right| = \frac{(1 - s\kappa)^3}{1 - s}, \quad (\kappa \leq 1). \quad (8)$$

For any fixed κ, γ, and a varying s, the resulting κ_{eff}, γ_{eff} from equation (7) lie on straight lines radiating from (1,0). This is the reason for the higher concentration of points to the left and top of the right-hand panel of Fig. 1 (see also fig. 1 of Vernardos & Fluke 2014b).

Next, a constrained rather than free variation of the κ, γ values for each image is examined (CON7). Two new parameters are used, namely, the magnification (equation 6) and the displacement along a constant magnification contour, t_μ. In this way, the observationally motivated constraint on μ is easily achieved by allowing its value for one image to vary slightly with respect to the fixed magnification of the other image. Varying μ between 0.9 and 0.96 × f_{base} (the baseline magnification without microlensing) in steps of 0.01, and t on fixed

intervals, creates a rectangular regular grid for both parameters. Transforming between (t, μ) and (κ, γ) is trivial, however, there is a volume, or weight, associated with each resulting κ, γ location due to the coordinate transformation

$$\left| \det \frac{\partial(\kappa, \gamma)}{\partial(\mu, t)} \right| = \frac{[(1 - \kappa)^2 + \gamma^2]^2}{2\gamma}. \quad (9)$$

To obtain the probabilities on this new grid of κ, γ under the assumed constraint on μ, the likelihood values of CON6 (left-hand panel of Fig. 1) are interpolated using the natural neighbour interpolation technique (Sibson 1981). In Fig. 2, the constrained probability distributions of κ, γ, s are shown (CON7), multiplied by the correct weight and marginalized over the accretion disc parameters r_0 and ν, for varying κ_{min}, γ_{min} (left-hand panel) and κ_{sad}, γ_{sad} (right-hand panel). As expected, the $\kappa-\gamma$ joint probability contours follow the shape of constant magnification contours [e.g. see fig. 1, fig. 3 of Witt et al. (1995), or fig. 7b of Vernardos & Fluke (2014b)].

In the top panel of Fig. 3 we show 100 pairs of images, coloured according to their probability (CON8). In this case, the assumption of keeping one of the two images fixed to κ_{ML13}, γ_{ML13} has been dropped, but the constraint of the pair having a magnification ratio of f_{base} has been retained. Witt et al. (1995) have investigated singular spherical potentials for the lens having a convergence as a function of radius r of the form

$$\kappa(r) = \frac{\beta}{2} \left(\frac{b}{r} \right)^{2-\beta}, \quad (10)$$

where β is the slope of the mass distribution (or potential, with $\beta = 1$ for a SIS model), and b is a scaling factor related to the Einstein

---

[5]The likelihood in the left-hand panel of Fig. 1 is collapsed with respect to s; for each κ, γ it is the sum of all the individual likelihoods for different s. Having the likelihood as a function of κ, γ, and s allows to plot the right-hand panel of Fig. 1.
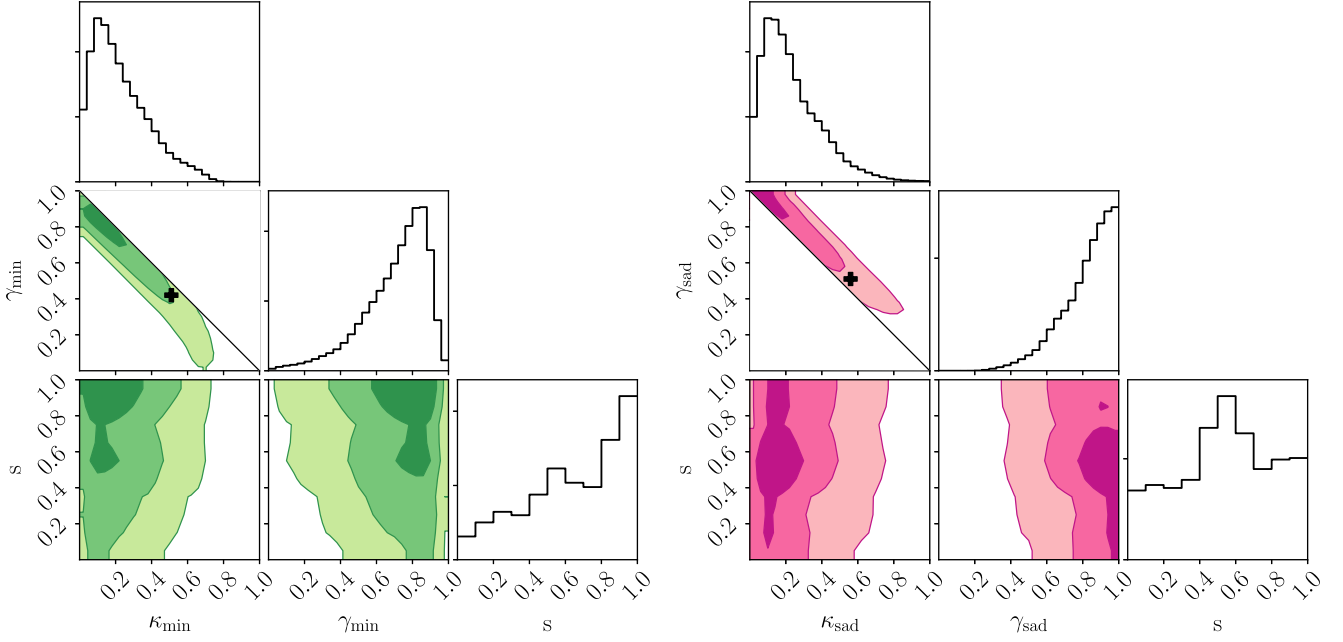
Figure 2. Constrained probability densities and histograms for κ_{min}, γ_{min}, s and κ_{sad}, γ_{sad}, s (CON7), marginalized over the accretion disc parameters r_0 and ν. Contours are drawn at the 68, 95, and 99 per cent confidence intervals. Crosses indicate the location of the κ_{ML13}, γ_{ML13} values.

radius of the lens, and derived the theoretical result

$$\gamma = \frac{4 - \beta}{\beta} \kappa - 1. \tag{11}$$

We have used this relation to loosely correlate each pair shown in Fig. 3 with the slope of such a fiducial potential for the lens (a practical reason for this 'looseness' is the finite and irregular grid of available magnification maps in the κ, γ parameter space). By fitting equation (11) to each pair, the probability density of the slope β is derived and shown in the bottom panel of Fig. 3. The expectation value of β is $0.79^{+0.60}_{-0.53}$ at the 68 per cent confidence interval (which is not really meaningful, given the flatness of the distribution in the lower panel of Fig. 3). Transforming this to probability distributions for κ and γ (as in the last column of Table 2), the following weights have to be used

$$\left|\frac{\partial \kappa}{\partial \beta}\right| = \frac{(\kappa + \gamma + 1)^2}{4(\gamma + 1)}, \tag{12}$$

$$\left|\frac{\partial \gamma}{\partial \beta}\right| = \frac{(\kappa + \gamma + 1)^2}{4\kappa}. \tag{13}$$

The marginalized probabilities of the accretion disc parameters r_0 and ν are shown in Fig. 4 for all sets of results. Interestingly, the shape of the probability contours and histograms is almost identical.

Finally, the expectation values for the accretion disc and the lens parameters from all four sets of results are shown in Table 2. Introducing a logarithmic prior on s (as discussed in Section 2.3) has a minor effect on these values: slightly lower values are preferred for the derived κ_{min} and κ_{sad}, values between 0.3 and 0.4 are preferred for s, and slightly higher values between 1.7 and 1.8 are preferred for ν. However, in both cases the derived values are consistent within their confidence intervals.

3.1 The computations

The most computationally demanding part of the simulations undertaken in this paper is generating the microlensing magnification maps for a wide range of κ, γ, and s. However, this task has been already accomplished by the GERLUMPH parameter survey, which has made available more than 70 000 magnification maps in the targeted part of parameter space (see Vernardos et al. 2014; Vernardos & Fluke 2014a). The number of individual magnification maps used in the case of a fixed image was 10: a single κ, γ location with 10 different values of s. A set of 1400 maps (140 κ_{sad}, γ_{sad} locations) were used for a varying minimum image, and 3000 maps (300 κ_{min}, γ_{min} locations) for a varying saddle point. To obtain the probability of the 100 pairs shown in Fig. 3, 2000 maps were used. The total number of magnification maps used is 6400, which would have taken approx. 1830 d to generate on a single Graphics Processing Unit (GPU), or just 29 d using the GPU-Supercomputer for Theoretical Astrophysics Research (gSTAR). For comparison, the remaining part of the computations, i.e. the convolutions between maps and source profiles described below, took 10 d on gSTAR.

All the results share a common grid of the accretion disc parameters r_0 and ν. This grid contains 192 unique combinations, which, from equation (1), produce 768 different accretion disc sizes.[6] From these, only the 209 sizes that correspond to accretion disc profiles smaller than $16 \times R_{Ein}$ – the adopted no-microlensing limit – were convolved with magnification maps to extract simulated flux ratios, while the rest have been given a fixed ratio equal to f_{base}.

A total of 26 752 000 convolutions between 10 000²-pixel maps and profiles were performed (maps for both images had to be convolved with the same profile), using multiple GPUs on gSTAR over a period of 10 d. Our final results consist of 12 288 000 likelihood evaluations (equation 3), for each of which we computed 10^8 χ^2

---

[6]The possible case of a combination of r_0, ν, and λ resulting in practically the same r from equation (1) is disregarded.
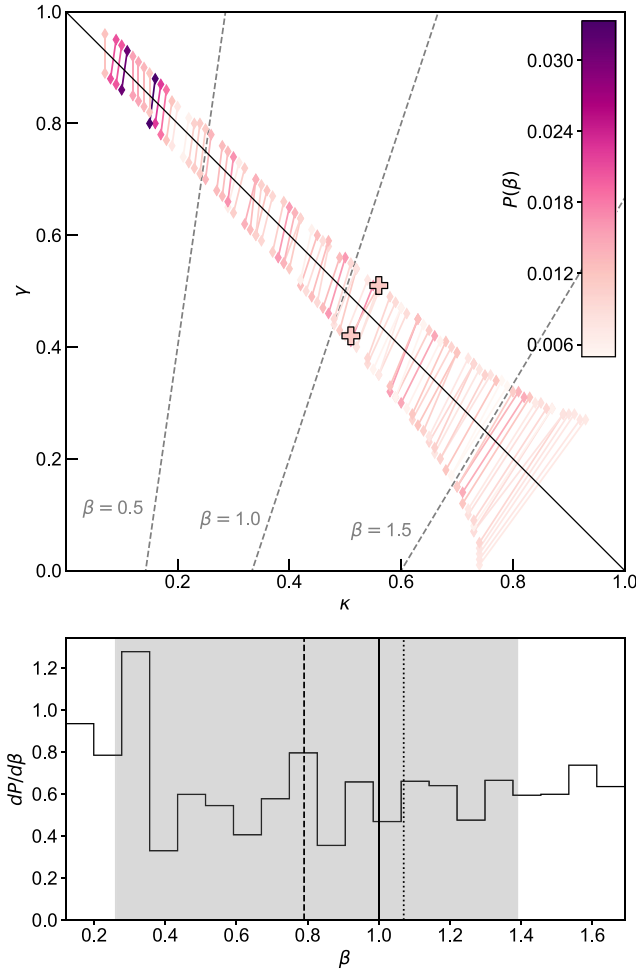
Figure 3. Top: pairs of minimum – saddle-point images in the parameter space, with darker (lighter) colours indicating higher (lower) probability (CON8). Crosses mark the κ_{ML13}, γ_{ML13} values (REF). The dashed lines correspond to equation (11) for specific values of β, as in fig. 1 of Witt, Mao & Schechter (1995). Bottom: probability density of the slope of a fiducial spherical potential for the lens, obtained by fitting equation (11) to the pairs shown in the top panel. The vertical solid line indicates the case of an isothermal potential ($\beta = 1$), the dotted line shows the slope value obtained by fitting κ_{ML13}, γ_{ML13} for the two images, the dashed line the value of $\beta = 0.79$ obtained from CON8 and the grey shaded area its 68 per cent confidence interval.

terms either by calculating f^{sim} in equation (4) as described, or by setting it equal to f_{base}.

4 DISCUSSION AND CONCLUSIONS

Despite the extreme variations in κ, γ, leading to dramatically different magnification maps with respect to caustic structure and magnification probability distribution, in all the examined cases the same accretion disc constraints are derived, as shown in the last two rows of Table 2 and in Fig. 4. This apparent independence of the accretion disc on the macromodel supports the findings of Bate et al. (2018): the derived accretion disc properties appear to be tightly connected to the observed data, in this case, the large chromatic variations of the flux ratios. The macromodel seems to be playing an insignificant role, at least for MG 0414+0534 examined here and
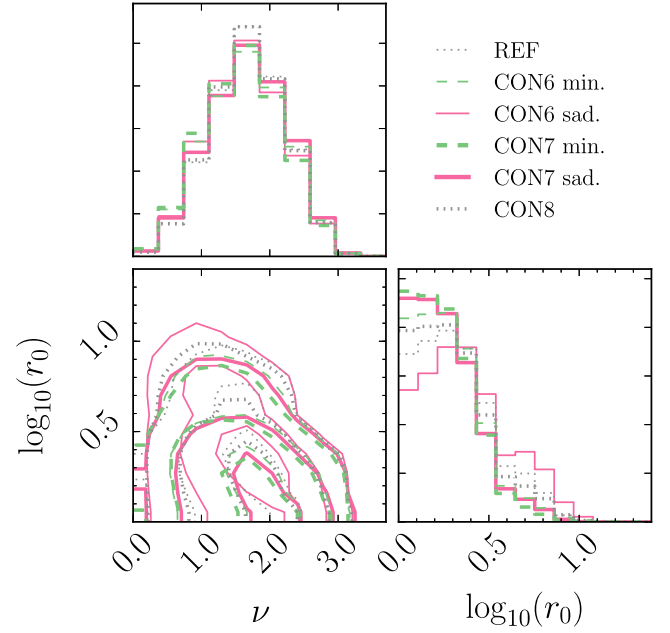

Figure 4. Probability density and histograms for the accretion disc parameters r_0 (in light-days) and ν, corresponding to the size of the accretion disc at the rest wavelength $\lambda_0 = 1026$Å and its power-law dependence on wavelength (see equation 11). All the different sets of results presented here are shown, marginalized over κ, γ, and s whenever applicable. Contours are drawn at the 68, 95, and 99 per cent confidence intervals.

the given extreme chromatic variation of the flux ratios (Bate et al. 2018).

The accretion disc constraints of Table 2 are consistent with Bate et al. (2008) for the size and the slope parameters of equation (1), while for the slope the agreement with Bate et al. (2018) is marginal. The main reason for this is that they used maps with a width of $100R_{Ein}$, much wider than the $25R_{Ein}$ maps used here, allowing for the inclusion of larger sources ($>16R_{Ein}$) in calculating the likelihood surface of Fig. 4. This and a number of other effects have been identified to influence the derived accretion disc constraints to a smaller or larger extent: the size of the effective map, the value of the baseline ratio, f_{base}, and its uncertainty, the number of simulated ratios between maps, and the way these were selected (from pixels on a fixed grid, in random locations, etc.). These potential sources of bias will be examined in future work.

More than half of the matter at the location of the examined image pair is found to be in the form of a smooth component, regardless of the macromodel. This is not surprizing because the multiple images form at the outskirts of the lensing galaxy, where the stellar density is expected to be low. In fact, higher smooth matter fractions can be invoked to explain the observed flux ratio anomaly, usually manifesting itself as a demagnified saddle point (Schechter & Wambsganss 2002; Vernardos et al. 2014). The value of s from Bate et al. (2018) is $0.5^{+0.3}_{-0.3}$ (N. Bate, private communication), consistent with the values of Table 2. Bate et al. (2011) find a value of 0.8 for MG 0414+0534, Pooley et al. (2012) find a higher value of 0.93, while (Jiménez-Vicente et al. 2015) find a value of 0.8 by examining a collection of 27 image pairs of lensed quasars. However, the uncertainty on s (Table 2) is quite large in all cases, indicating basically flat distributions.

Based purely on the microlensing observations, without using any other kind of data, is there anything to be said about the lens

mass model? The inferred values of κ_{min}, γ_{min}, and κ_{sad}, γ_{sad}, more often disagree with the macromodel of MacLeod et al. (2013) than agree. Of course, one has to take into account the largely underconstrained nature of the problem: the model has seven free parameters and the result sets CON6, CON7, and CON8 use six, seven, and eight constraints, respectively. Therefore, the values and confidence intervals derived for κ, γ in Table 2 should be taken cautiously. In general, for the observed flux ratios in Table 1, and without any information on the macromodel (derived from imaging data), it seems that steeper mass distributions than isothermal are favoured, leading to lower κ and higher γ values at the location of the close pair of images (see Figs 2 and 3).

It is interesting to investigate the convergence of the solutions of the model as more observational constraints are used. The method introduced in this paper would be straightforward to apply by adding more terms in equation (4) and assuming the flux ratios from different observational epochs are uncorrelated.[7] Additionally, the effectiveness of using flux ratios with different (smaller) chromatic variations should be tested. In fact, if each close pair image configuration can be associated with distinct flux ratio properties, then the solutions should converge to the correct κ, γ. This will be investigated in future work using mock data for several systems with different κ, γ (similarly to what is suggested in Bate et al. 2018).

A similar ansatz, i.e. finding the macromodel parameters based on microlensing observables, can be suggested and tested in the case of light curves. The method presented here can be modified accordingly to use light-curve data, and the model expanded to include additional parameters such as the velocities of the observer, source, and lens, etc. However, this would require a careful selection of priors on the new parameters and an understanding of their effect in the interpretation of the results. This is another path of exploration spurring from this work.

Finally, it is relatively straightforward to combine the analysis presented here with techniques that fit the macromodel to imaging data; it would be a simple addition of flux ratio and image position χ^2 terms. Such an approach would be meaningful if the solutions of the method presented here are indeed shown to converge to useful values of κ, γ, and could be proven valuable in disentangling microlensing effects from the presence of substructure in the lens. Combining this method with imaging data would be easier than with light curves.

In this paper, a joint analysis of the lens macromodel and the accretion disc was performed for the first time, driven solely by microlensing flux ratio data. The derived accretion disc constraints were proven to be quite robust under broad variations of the κ, γ for each image. With the method and machinery presented in this study, one can envisage simultaneous analysis of different kinds of available observations, deriving constraints on the lens mass and accretion disc models of a lensed quasar. The cornerstone for such multicomponent modelling approaches is a readily available collection of magnification maps, like GERLUMPH, which removes the need of the huge amount of computations associated with generating them. The future for lensing studies driven by a variety of available observational data modelled in the same framework looks promising.

---

[7]This means that the source will have to move across the sky by a distance corresponding to at least its own size. Mosquera & Kochanek (2011) calculate a median source crossing time-scale of 7.3 months based on a sample of 87 lensed quasars.

REFERENCES

Bate N. F., Fluke C. J., 2012, ApJ, 744, 90
Bate N. F., Floyd D. J. E., Webster R. L., Wyithe J. S. B., 2008, MNRAS, 391, 1955
Bate N. F., Floyd D. J. E., Webster R. L., Wyithe J. S. B., 2011, ApJ, 731, 71
Bate N. F., Vernardos G., O'Dowd M. J., Neri-Larios M. D., 2018, MNRAS, 479, 4796
Behroozi P. S., Conroy C., Wechsler R. H., 2010, ApJ, 717, 379
Blackburne J. A., Pooley D., Rappaport S., Schechter P. L., 2011, ApJ, 729, 34
Bourne M. A., Sijacki D., 2017, MNRAS, 472, 4707
Chartas G., Kochanek C. S., Dai X., Poindexter S., Garmire G., 2009, ApJ, 693, 174
Conroy C., Wechsler R. H., 2009, ApJ, 696, 620
Cowley M. J. et al., 2018, MNRAS, 473, 3710
Dai X., Kochanek C. S., Chartas G., Kozłowski S., Morgan C. W., Garmire G., Agol E., 2010, ApJ, 709, 278
Dalal N., Kochanek C. S., 2002, ApJ, 572, 25
Falco E. E., Gorenstein V. M., Shapiro I. I., 1985, ApJ, 289, L1
Floyd D. J. E., Bate N. F., Webster R. L., 2009, MNRAS, 398, 233
Foxley-Marrable M., Collett T. E., Vernardos G., Goldstein D. A., Bacon D., 2018, MNRAS, 11, 1
Guerras E., Mediavilla E., Jimenez-Vicente J., Kochanek C. S., Muñoz J. A., Falco E., Motta V., 2013, ApJ, 764, 160
Hewitt J. N., Turner E. L., Lawrence C. R., Schneider D. P., Brody J. P., 1992, AJ, 104, 968
Jimenez-Vicente J., Mediavilla E., Kochanek C. S., Muñoz J. A., Motta V., Falco E., Mosquera A. M., 2014, ApJ, 783, 47
Jiménez-Vicente J., Mediavilla E., Kochanek C. S., Muñoz J. A., 2015, ApJ, 799, 149
Kayser R., Refsdal S., Stabell R., 1986, A&A, 166, 36
Keeton C. R., 2001, preprint (astro-ph/0102340)
Kochanek C. S., Morgan N. D., Falco E. E., McLeod B. A., Winn J. N., Dembicky J., Ketzeback B., 2006, ApJ, 640, 47
Lawrence C. R., Elston R., Januzzi B. T., Turner E. L., 1995, AJ, 110, 2570
Leier D., Ferreras I., Saha P., Charlot S., Bruzual G., La Barbera F., 2016, MNRAS, 459, 3677
MacLeod C. L., Jones R., Agol E., Kochanek C. S., 2013, ApJ, 773, 35
MacLeod C. L. et al., 2015, ApJ, 806, 258
Mao S., Schneider P., 1998, MNRAS, 295, 587
Metcalf R. B., Madau P., 2001, ApJ, 563, 9
Minezaki T., Chiba M., Kashikawa N., Inoue K. T., Kataza H., 2009, ApJ, 697, 610
Morgan C. W., Kochanek C. S., Morgan N. D., Falco E. E., 2010, ApJ, 712, 1129
Mortonson M. J., Schechter P. L., Wambsganss J., 2005, ApJ, 628, 594
Mosquera A. M., Kochanek C. S., 2011, ApJ, 738, 96
Moster B. P., Somerville R. S., Maulbetsch C., Van Den Bosch F. C., MacCiò A. V., Naab T., Oser L., 2010, ApJ, 710, 903
O'Dowd M. J., Bate N. F., Webster R. L., Labrie K., Rogers J., 2015, ApJ, 813, 62
Oguri M., Rusu C. E., Falco E. E., 2014, MNRAS, 439, 2494
Paczynski B., 1986, ApJ, 301, 503
Pooley D., Blackburne J. A., Rappaport S., Schechter P. L., 2007, ApJ, 661, 19

Pooley D., Rappaport S., Blackburne J. A., Schechter P. L., Wambsganss J., 2012, ApJ, 744, 111

Rojas K., Motta V., Mediavilla E., Falco E., Jiménez-Vicente J., Muñoz J. A., 2014, ApJ, 797, 61

Rosas-Guevara Y. M. et al., 2015, MNRAS, 454, 1038

Schechter P. L., Wambsganss J., 2002, ApJ, 580, 685

Schneider P., Kochanek C. S., Wambsganss J., 2006, in Meylan G., Jetzer P., North P., eds, Saas-Fee Advanced Course, Vol. 33, Gravitational Lensing: Strong, Weak, Micro. Springer, Berlin

Shakura N., Sunyaev R., 1973, A&A, 24, 337

Sibson R., 1981, in Barnett V., ed., Interpreting Multivariate Data. Wiley, Chichester West Sussex, New York, p. 21

Terrazas B. A., Bell E. F., Woo J., Henriques B. M. B., 2017, ApJ, 844, 170

Tonry J. L., Kochanek C. S., 1999, AJ, 117, 2034

Treu T., Auger M. W., Koopmans L. V. E., Gavazzi R., Marshall P. J., Bolton A. S., 2010, ApJ, 709, 1195

Vernardos G., Fluke C. J., 2014a, Astron. Comput., 6, 1

Vernardos G., Fluke C. J., 2014b, MNRAS, 445, 1223

Vernardos G., Fluke C. J., Bate N. F., Croton D. J., 2014, ApJS, 211, 16

Witt H., Mao S., Schechter P., 1995, ApJ, 443, 18

This paper has been typeset from a TEX/LATEX file prepared by the author.